Earth's Future

RESEARCH ARTICLE
10.1029/2025EF007133

Escalating Extreme River Discharge Events Driven by Precipitation Changes in the Yangtze River Basin

Xiaoke Xu[1], Anning Huang[2,3], Yinghong Jing[1], Chunlei Gu[2], Xiaojun She[1], and Yao Li[1]

[1]Chongqing Jinfo Mountain Karst Ecosystem National Observation and Research Station, Chongqing Engineering Research Center for Remote Sensing Big Data Application, School of Geographical Sciences, Southwest University, Chongqing, China, [2]School of Atmospheric Sciences, Nanjing University, Nanjing, China, [3]Plateau Atmosphere and Environment Key Laboratory of Sichuan Province, College of Atmospheric Sciences, Chengdu University of Information Technology, Chengdu, China

Key Points:

- The occurrence of extreme river discharge events (ERDEs) increased significantly across the Yangtze River Basin from 2000 to 2019
- These ERDEs were associated with distinct precipitation patterns—upstream, local, and overlapped
- Meteorological systems causing these precipitation patterns can be detected 72–120 hr before ERDEs in upstream, local, or junction areas

Correspondence to:
Y. Li,
liyao7@swu.edu.cn

Citation:
Xu, X., Huang, A., Jing, Y., Gu, C., She, X., & Li, Y. (2026). Escalating extreme river discharge events driven by precipitation changes in the Yangtze River Basin. *Earth's Future*, *14*, e2025EF007133. https://doi.org/10.1029/2025EF007133

Received 23 AUG 2025
Accepted 9 MAR 2026

Author Contributions:
Conceptualization: Xiaoke Xu, Anning Huang, Yao Li
Data curation: Xiaoke Xu
Formal analysis: Xiaoke Xu, Yao Li
Funding acquisition: Yao Li
Investigation: Xiaoke Xu
Methodology: Xiaoke Xu, Yinghong Jing, Chunlei Gu
Project administration: Yao Li
Resources: Yao Li
Supervision: Anning Huang, Yao Li
Validation: Xiaoke Xu
Visualization: Xiaoke Xu
Writing – original draft: Xiaoke Xu
Writing – review & editing: Anning Huang, Yinghong Jing, Chunlei Gu, Xiaojun She, Yao Li

Abstract Extreme river discharge events (ERDEs) directly induce catastrophic floods, posing severe threats to human life and infrastructure. Understanding the precipitation patterns that precede ERDEs is critical for identifying early flood warnings. This study investigated the spatiotemporal characteristics of 3-hourly ERDEs across the Yangtze River Basin (YRB) from 2000 to 2019. A Random Forest model was employed to explore the nonlinear relationships between the cumulative precipitation in local/upstream regions and the number of ERDEs, aiming to identify precipitation patterns and the associated atmospheric processes. The results reveal that ERDEs predominantly occurred in the upper reaches of the eastern Tibetan Plateau and the middle to lower YRB, spanning from March to November, with a peak in July. A significant increasing trend in the occurrence of ERDEs was observed over the 20 years in the YRB. In the eastern Tibetan Plateau and the Dongting Lake Plain, ERDEs were primarily affected by upstream precipitation, associated with the plateau vortex and backwards-tilting trough. In contrast, ERDEs in the western Sichuan Basin and Poyang Lake Plain were mainly driven by local precipitation, linked to the forward-tilting trough and Jianghuai cyclone. Furthermore, regions such as the western Sichuan Plateau, central-eastern Sichuan Basin, Wushan Mountain range, and lower Yangtze River Plain were influenced by both upstream and local precipitation, which were attributed to the westerly trough, southwest vortex, double-vortex, and convective system on the edge of the Northwestern Pacific Subtropical High, respectively. This study presents a novel perspective on identifying early warning signals of flood risk across YRB.

Plain Language Summary Extreme river discharge events (ERDEs) serve as precursors to flood disasters. Understanding precipitation patterns and associated atmospheric processes that cause ERDEs is crucial for early flood warning systems. This study examined ERDEs in China's Yangtze River Basin (YRB) during 2000–2019 to explore the relationship between ERDEs and local/upstream precipitation. ERDEs increased over the 20-year period, occurring most frequently in the Eastern Tibetan Plateau and the middle and lower YRB, with a peak in July. In regions such as the eastern Tibetan Plateau and Dongting Lake, upstream rainfall linked to weather systems, such as the plateau vortex, is the primary driver. In contrast, areas such as the western Sichuan Basin and Poyang Lake are mainly influenced by local rainfall associated with systems like the Jianghuai cyclone. Some regions, including the Wushan Mountains and the lower YRB, are affected by both local and upstream rainfall, driven by the combined influence of westerly winds, vortices, and convective systems near the edge of the Northwestern Pacific Subtropical High. These findings enhance understanding of the rainfall patterns underlying ERDEs and provide valuable insights for improving the accuracy and timeliness of regional flood early warning systems.

1. Introduction

Extreme river discharge events (ERDEs), which often manifest as catastrophic floods, pose significant threats to human life, infrastructure, and ecosystems (Camilloni & Barros, 2003; Heinrich et al., 2023; Yin et al., 2018). As one of the most densely populated river basins in the world, the Yangtze River Basin (YRB) relies heavily on flood early warning systems to safeguard livelihoods and support sustainable regional economic development (Li & Zhao, 2022; Yu et al., 2023). YRB is among the regions in China experiencing the highest frequency of daily-scale ERDEs (Jia et al., 2022; Wei et al., 2020). In the middle and lower reaches, these events are commonly attributed to flat terrain and numerous tributaries (Ye et al., 2017; Yu et al., 2023). In contrast, daily-scale ERDEs

in the upper and middle reaches often lead to devastating floods due to the complex mountainous terrain and limited flood control infrastructure (Fang et al., 2018; Liu et al., 2019). These events primarily occur from June to September (Wang et al., 2022). In the context of global warming, sub-daily extreme precipitation events have become more frequent, thereby increasing the risk of ERDEs (Do et al., 2020; Li et al., 2017). However, most previous studies have focused predominantly on the daily scale (Durowoju et al., 2017; Kundzewicz et al., 2019). As a result, the detailed characteristics of sub-daily ERDEs and their relationship with precipitation remain unclear. Therefore, it is essential to investigate the fine-scale characteristics of ERDEs and improve the early warning capabilities for ERDEs in the YRB.

Precipitation is the primary trigger of ERDEs (Breinl et al., 2021; Wright et al., 2020). Previous studies have shown that ERDEs are most likely to occur within 5 days following heavy rainfall events (Tuel et al., 2021; Xu et al., 2018). This temporal window varies across regions and is influenced by the response of river runoff to both precipitation intensity and amount, exhibiting marked spatial heterogeneity across the YRB (Wang et al., 2021; Yu et al., 2023). For example, the upper reaches of the YRB respond more rapidly and intensely to heavy rainfall due to steep terrain, whereas the middle and lower reaches exhibit a more delayed response due to complex river networks and human influences (Chen et al., 2014; Wang et al., 2013). Under a 50-year extreme rainfall scenario, the relative rate of change in average daily river runoff decreases progressively from the upper to the lower reaches of the YRB (Gao et al., 2023). However, research on precipitation patterns preceding sub-daily ERDEs, particularly the influence of upstream and local precipitation, remains limited.

Understanding the meteorological mechanisms behind ERDEs is crucial for identifying potential early warning signals (Breugem et al., 2020; Xu et al., 2011). These meteorological mechanisms encompass anomalous large-scale atmospheric circulation (Nie & Sun, 2021; Xu et al., 2023), local thermodynamic and dynamic processes (Xu et al., 2024; Zhang et al., 2019), and land-atmosphere interactions (Hua et al., 2020; Kang et al., 2019). Atmospheric circulation anomalies associated with the El Niño-Southern Oscillation (ENSO) are a dominant climatic driver of frequent and intense precipitation events that may lead to ERDEs (Kundzewicz et al., 2020; Wei et al., 2020). Moreover, changes in the East Asian monsoon, tropical cyclones, and subtropical westerly jets significantly enhance precipitation and river discharge in China (Yang, Yang, et al., 2021). In local thermodynamic processes, a key contributor to persistent precipitation is anomalous local water vapor transport associated with mesoscale synoptic systems (Fu et al., 2011, 2015; Yang, Xia, et al., 2021). In terms of land-atmosphere interactions, large-scale topography can block convective systems and prolong precipitation duration, thereby increasing the likelihood of ERDEs (Bai et al., 2021; Zhang et al., 2021). While considerable progress has been made in understanding the mechanisms of extreme precipitation (Breugem et al., 2020), the atmospheric processes underlying ERDE-related precipitation patterns remain poorly understood. This gap poses substantial challenges for the practical identification and prediction of early warning signals.

With the rapid advancement of artificial intelligence, machine learning has been widely applied to monitor, attribute, and predict ERDEs based on its distinct advantages in feature extraction, adaptability, and computational efficiency (Li et al., 2022; Zhang et al., 2022; Zhao et al., 2022). Convolutional Neural Networks (Tavus et al., 2022), Multiple Linear Regression (Luu et al., 2019), Long Short-Term Memory (Ding et al., 2020), and Random Forest (RF) (Adikari et al., 2021) are among the most widely used algorithms in ERDEs and flood event research. Despite their lack of physical interpretability, machine learning methods have proven to be powerful tools for data fitting, feature classification, and trend forecasting (Prodhan et al., 2022).

Nevertheless, several questions remain insufficiently addressed in previous studies: (a) What are the fine-scale characteristics of sub-daily ERDEs in the YRB over the past two decades? (b) What precipitation patterns are responsible for triggering these ERDEs? and (c) What meteorological processes underlie these precipitation patterns? To address these questions, this study investigates the sub-daily characteristics of ERDEs, the associated precipitation patterns, and their underlying atmospheric processes using satellite observations and reanalysis data sets over the YRB from 2000 to 2019. The findings of this research enhance understanding of the precipitation mechanisms that trigger ERDEs and provide a scientific foundation for developing more accurate early warning systems in the YRB.

2. Data and Study Area

2.1. Data Sets

The data sets used in this study are described as follows:

1. River order and slope information were derived from the MERIT Hydro v07 Basins v01 data set, a global vector hydrographic database developed from the 90 m resolution MERIT-Hydro product (Yamazaki et al., 2019).
2. River discharge data were obtained from the Global Reach-Level 3-Hourly River Flood Reanalysis (GRFR) V1.0 data set from 2000 to 2019 (Yang, Pan, et al., 2021).
3. Precipitation data were sourced from the final run of the GPM-IMERG V06 data set, which provided half-hourly observations at a spatial resolution of 0.1° × 0.1° from 2000 to 2019 (Hou et al., 2014). GPM-IMERG has been widely used for precipitation monitoring over China and is well-suited for capturing the spatiotemporal characteristics of precipitation over the YRB (Li et al., 2024; Yang et al., 2020). To ensure consistency with the 3-hourly river discharge data, half-hourly precipitation was aggregated to 3-hr intervals (e.g., "00:00" corresponds to the period from 00:00 to 02:59). Following previous studies, we analyzed precipitation during the 5-day period prior to each ERDE (Deng et al., 2022; Tuel et al., 2021).
4. Historical flood event records were collected from the Global Natural Disaster Information Database (GNDID) (http://disaster.ncdc.ac.cn/#/root/view), maintained by the National Cryosphere Desert Data Center of China. These records were used as auxiliary information to verify the identification of ERDEs.
5. Atmospheric variables were from the fifth-generation ECMWF reanalysis data set (ERA5), with a spatial resolution of 0.25° and hourly temporal resolution, covering the period from 2000 to 2019 (Hersbach et al., 2023). Variables—including temperature, geopotential height, specific humidity, wind, and pressure—were resampled to 3-hourly intervals to be consistent with the GRFR data set.
6. Topography information was derived from the Shuttle Radar Topography Mission (SRTM) Digital Elevation Database v4.1 with a spatial resolution of 3 arc s (~90 m) (Jarvis et al., 2008), which was accessed via Google Earth Engine.

2.2. Study Area

Based on the MERIT hydrographic data set, rivers classified as level 4 and above were selected as the primary focus of this study (Figure 1a). River gradients are steep in the upper reaches and gradually decrease downstream. For regional analysis, the YRB was divided into nine regions according to river slope and elevation (Figure 1b): the source region of the Yangtze River (Reg1), Eastern Tibetan Plateau (Reg2), Western Sichuan Plateau (Reg3), Western Sichuan Basin (Reg4), Central-eastern Sichuan Basin (Reg5), Wushan Mountain Range (Reg6), Dongting Lake Plain (Reg7), Poyang Lake Plain (Reg8), and Lower Yangtze River Plain (Reg9). This classification provides a basis for examining the spatial heterogeneity of ERDEs across different geomorphological and hydrological settings within the basin.

3. Methods

3.1. Definition of Extreme River Discharge Event (ERDE)

Because the GRFR data set contains numerous river discharge records unrelated to flood events, we calculated the 3-hourly river discharge percentiles (90th, 95th, and 99th) for each river reach and validated the identified flood events against the GNDID data set. Flood events defined by discharge exceeding the 95th percentile showed the closest agreement with GNDID records. Therefore, events identified using this percentile threshold were referred to as ERDEs.

3.2. Calculation of Meteorological Variables

To analyze the atmospheric processes associated with precipitation patterns responsible for ERDEs, three key meteorological variables were employed in this study: water vapor flux (WVF), horizontal divergence, and pseudo-equivalent potential temperature (PEPT).

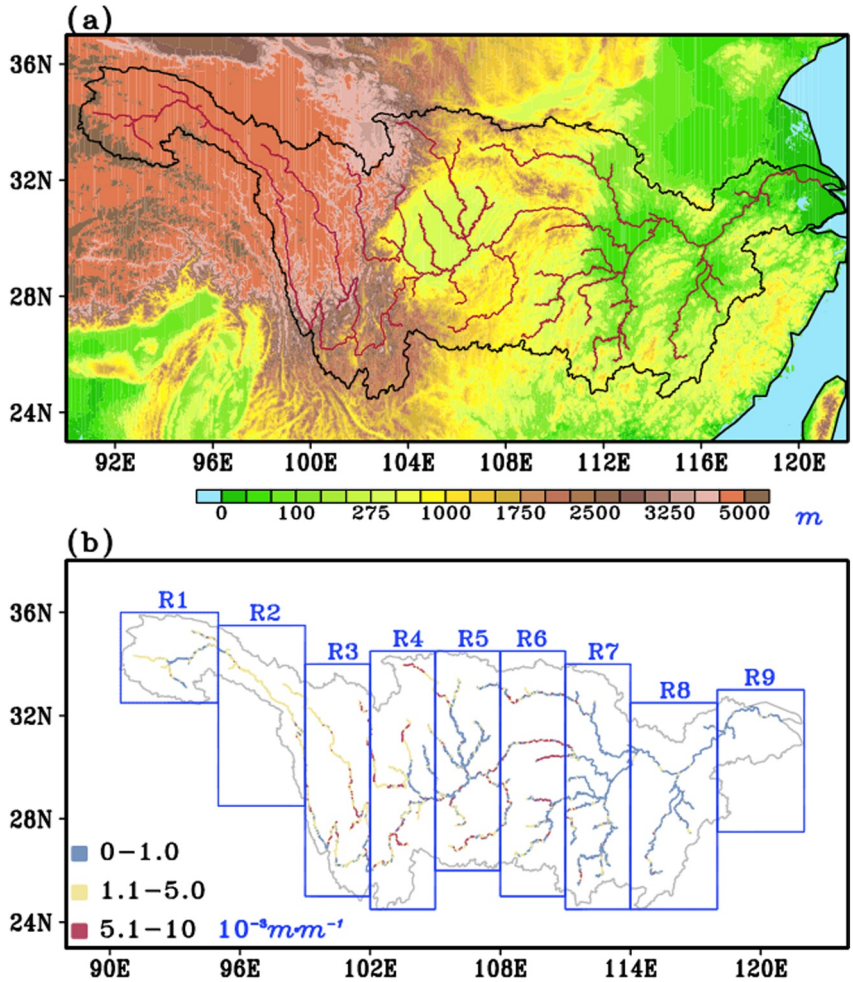

Figure 1. (a) Terrain elevation across the Yangtze River Basin and rivers classified above level 4 based on the MERIT data set; (b) Delineation of regions and corresponding river slopes. River slope is defined as the elevation drop per unit horizontal distance (10^{-3} m m^{-1}).

WVF (in units of kg · m^{-1} · s^{-1}) reflects the intensity and direction of water vapor transport within the atmosphere (Simmonds et al., 1999). In this study, vertically integrated WVF from the surface to 300 hPa was calculated to represent the change in water vapor throughout the entire layer.

$$\mathrm{WVF} = \frac{1}{g}\int_{Ps}^{300\ \mathrm{hPa}} \vec{V} \cdot q\, dp \tag{1}$$

where g, P_s, $\vec{V}, q, dp$ symbolizes the gravity acceleration, surface pressure, wind vector, specific humidity, and the change in air pressure in the vertical direction, respectively.

Horizontal divergence measures the extent to which the wind field converges or diverges at a given horizontal level. It is defined as:

$$\nabla_H \cdot \vec{V} = \frac{\partial u}{\partial x} + \frac{\partial v}{\partial y} \tag{2}$$

where ∇_H denotes the horizontal gradient operator and $\vec{V}$ represents the horizontal wind vector. u and v signify the eastward and northward components of the horizontal velocity, respectively. The unit of horizontal divergence

($\nabla_H \cdot \vec{V}$) is $10^{-5} \cdot s^{-1}$ in this study. Positive divergence values indicate horizontal convergence of wind, which promotes upward motion and increases the likelihood of precipitation.

PEPT is a thermodynamic variable that considers temperature, pressure, and humidity, serving as an indicator of atmospheric stability. It can be calculated as:

$$\theta = T_0\left(\frac{1000}{P_0}\right)^{0.286} + \frac{L_{qs}}{C_{pm}} \tag{3}$$

where θ is the PEPT, with units in K. $T_0 = T(1 + 0.61q)$ is the virtual temperature considering the effect of water vapor, where T is the air temperature and q is the specific humidity. P_0 is the standard atmospheric pressure. L_{qs} is the latent heat of saturated water vapor, which is approximately $2.5 \times 106\ J\ kg^{-1}$. C_{pm} represents the specific heat capacity of wet air at a constant pressure of $1005\ J\ kg^{-1}\ K^{-1}$. High PEPT values indicate the conveyor belt of warm and humid air flow, and the ridge line of PEPT represents the moving direction of the weather system (Bolton, 1980).

3.3. Random Forest Model

The RF model is a robust ensemble learning algorithm that constructs multiple decision trees using bootstrap aggregation and integrates their outputs through majority voting for classification or averaging for regression (Belgiu & Drăguţ, 2016; Breiman, 2001). It is particularly effective for diverse data sets with complex nonlinear relationships, making it a powerful tool for both classification and regression tasks (Min et al., 2018; Prodhan et al., 2022). In this study, the RF model was employed to extract nonlinear relationships between cumulative precipitation and ERDEs, aiming to identify dominant precipitation patterns associated with these events.

3.3.1. Overall Framework

The specific inputs and outputs of the RF model can be expressed as follows:

$$\begin{aligned} \mathrm{Num}_n &= \mathrm{RF}_n(\mathrm{PL}t_m, \mathrm{PU}t_m), n = 2, \ldots, 9 \\ t_m &= 0h, 3h, 6h, 12h, 24h, 48h, 72h, 96h, 120h \end{aligned} \tag{4}$$

where Num_n denotes the number of cumulative ERDEs in the region n, used as the target variable. $\mathrm{PL}t_m$ and $\mathrm{PU}t_m$ represent the regionally and temporally cumulative precipitation amount in the local and its adjacent upstream regions from 120 to t_m hours prior to ERDE occurrence, used as the input features (Figure 2a). For example, PU72h represents regionally cumulative precipitation in the upstream region during the period from 120 to 72 hr before an ERDE. Note that PL120h and PU120h refer to regionally cumulative precipitation in the local and upstream regions, respectively, during the initial 3-hr period within the 120 hr preceding an ERDE. A total of 18 variables from each region are input into the RF model as feature variables. Because Reg1 has no upstream region, the analysis is limited to eight regions (Reg2–Reg9). The output variable represents the predicted cumulative number of ERDE occurrences for each region. It should be noted that the RF model captures contemporaneous relationships between cumulative precipitation and the frequency of ERDE occurrences, rather than temporal trends in these relationships.

3.3.2. Experimental Strategy

The RF model was implemented with 200 trees, an unconstrained maximum depth, and a random seed of 42; all other parameters were set to their default values. The model was trained and validated using 10-fold cross-validation, in which all samples were randomly divided into 10 equal subsets. In each iteration, one subset served as the validation set while the remaining nine were used for training. This procedure was repeated 10 times, ensuring that all data points contributed to both training and validation (Figures 2b and 2c).

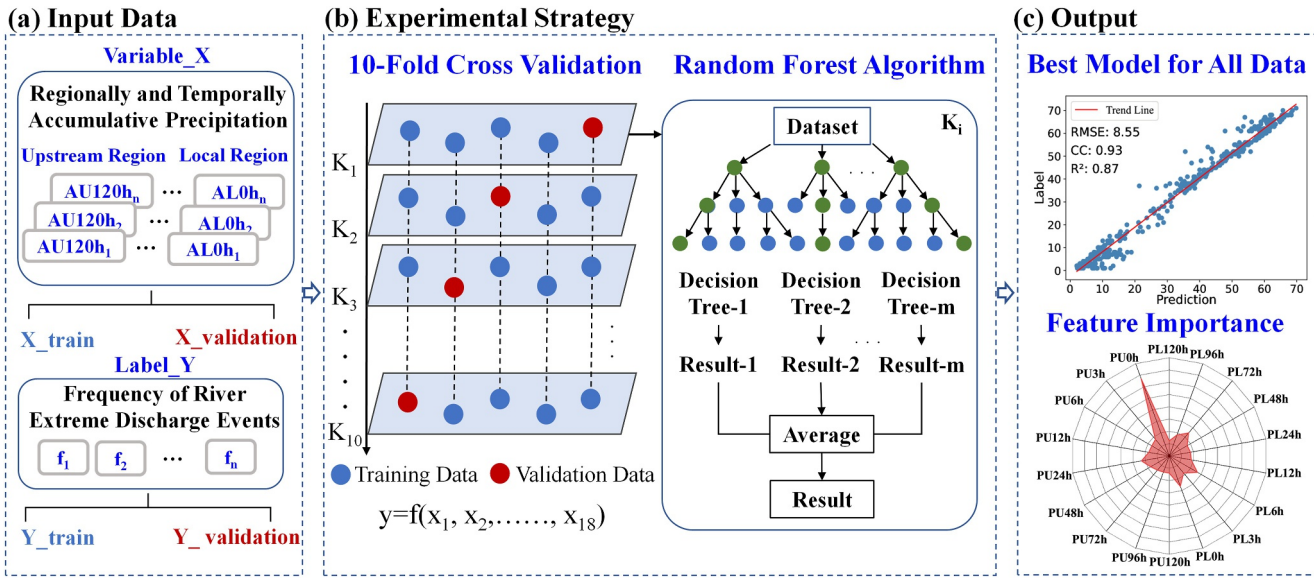

Figure 2. The Random Forest model and 10-fold cross-validation method for assessing the precipitation patterns responsible for the ERDEs over the Yangtze River Basin.

3.3.3. Model Evaluation and Analysis

Model performance was evaluated using the correlation coefficient (CC), coefficient of determination (R^2), and root-mean-square error (RMSE). After identifying the optimal model, predictions were generated using the complete set of input features. To understand the drivers of ERDEs, feature importance analysis was conducted to assess the relative contribution of each input variable to the output. This analysis helped determine whether ERDEs in each region were primarily influenced by local or upstream precipitation, or both.

4. Results and Discussion

4.1. Spatiotemporal Distribution of ERDEs Over YRB

ERDEs in the YRB exhibited pronounced temporal variation and spatial heterogeneity during 2000–2019. The 95th percentile threshold of river discharge revealed a distinct west-low to east-high spatial gradient along the Yangtze River (Figure 3a). ERDEs occurred most frequently along the mainstream in the Eastern Tibetan Plateau (Reg2), in tributaries of the Central-eastern Sichuan Basin (Reg5), in the northern tributaries of the Wushan Mountain Range (Reg6), and across the middle and lower Yangtze plains (Reg7–Reg9). In these areas, the cumulative number of ERDE occurrences exceeded 93 events, based on aggregated counts across river segments during the study period (Figure 3b). In contrast, the Western Sichuan Plateau (Reg3), Western Sichuan Basin (Reg4), and the southern part of Wushan Mountain Range (Reg6) experienced substantially fewer ERDEs (55–77 events). The regionally mean number of ERDE occurrences was highest in the estuary region (Reg9) and lowest in the source region of the Yangtze River (Reg1) (Figure 3d). During ERDEs, the average discharge in the middle and lower reaches of the YRB surpassed that in the upper reaches (Figure 3c), primarily due to the presence of numerous tributaries and flat channel gradients. Temporally, ERDEs were observed from March to November, with a peak in summer, especially in July. Over the 20 years, the average number of ERDE occurrences in July reached 129.3 events over YRB (Figure 3e). Notably, the number of ERDE occurrences in the YRB increased significantly from 2000 to 2019 (Figure 3f). Given the intricate spatiotemporal distribution of ERDEs in the YRB, further clarification of the precipitation patterns that lead to ERDEs is warranted.

4.2. Spatial Distribution of ERDE-Related Precipitation Over the YRB

Precipitation is the most direct driver of ERDEs (Breugem et al., 2020; Wei et al., 2022). Figure 4 illustrates the spatial distribution of cumulative precipitation during the 5 days preceding ERDE occurrence. Precipitation during the initial 3-hr period within the 120 hr preceding an ERDE was predominantly concentrated east of 102°E

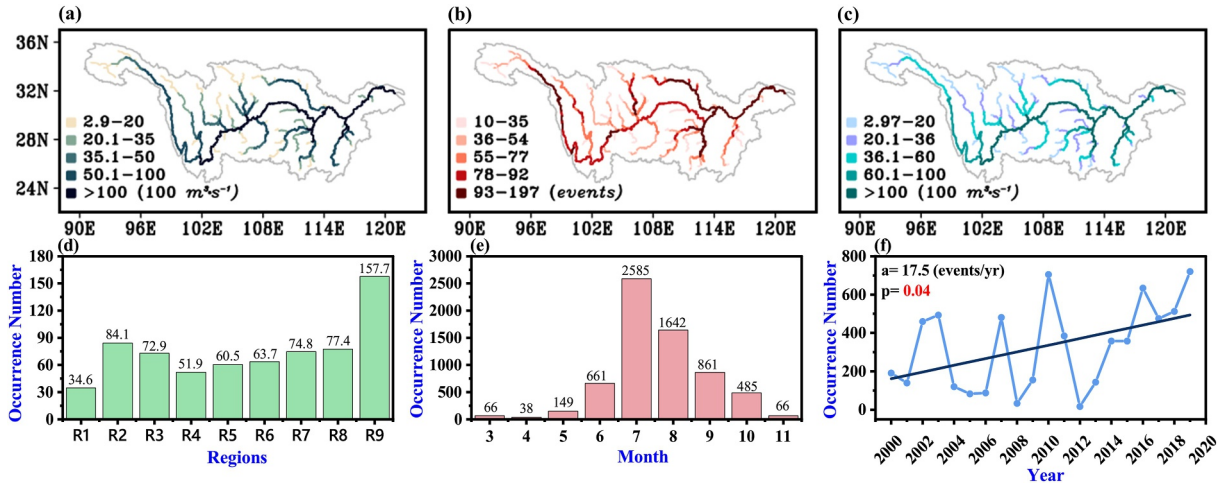

Figure 3. Temporal and spatial distribution of Extreme River Discharge Events (ERDEs) in the Yangtze River Basin from 2000 to 2019 based on the GRFR V1.0 data set. (a) Spatial distribution of the 3-hr 95th percentile threshold of river discharge, (b) cumulative number of ERDE occurrences, (c) average river discharge during ERDEs, (d) regional mean number of ERDE occurrences, (e) monthly cumulative number of ERDE occurrences (March–November), and (f) long-term trend in annual total number of ERDE occurrences.

(Reg4–Reg9) (Figure 4a). The cumulative precipitation referenced below was calculated from 120 hr prior to ERDE onset up to the specified time. At the 96 hr preceding ERDEs, cumulative precipitation was primarily concentrated over the northern part of the Central-eastern Sichuan Basin (Reg5), the southern Wushan Mountain Range (Reg6), and the middle and lower Yangtze plains (Reg7–Reg9) (Figure 4b). By 72 hr before ERDEs, cumulative precipitation strengthened along a west-to-east gradient, with a pronounced center (>35 mm) developing in northern Reg5 (Figure 4c). Persistent precipitation accumulation subsequently expanded across northern Reg5, southern Reg6, and Reg7–Reg9, with the maximum center exceeding 65 mm during the 48 to 12 hr prior to ERDEs (Figures 4d–4f). From 6 to 3 hr before ERDEs, the extensive precipitation zone over

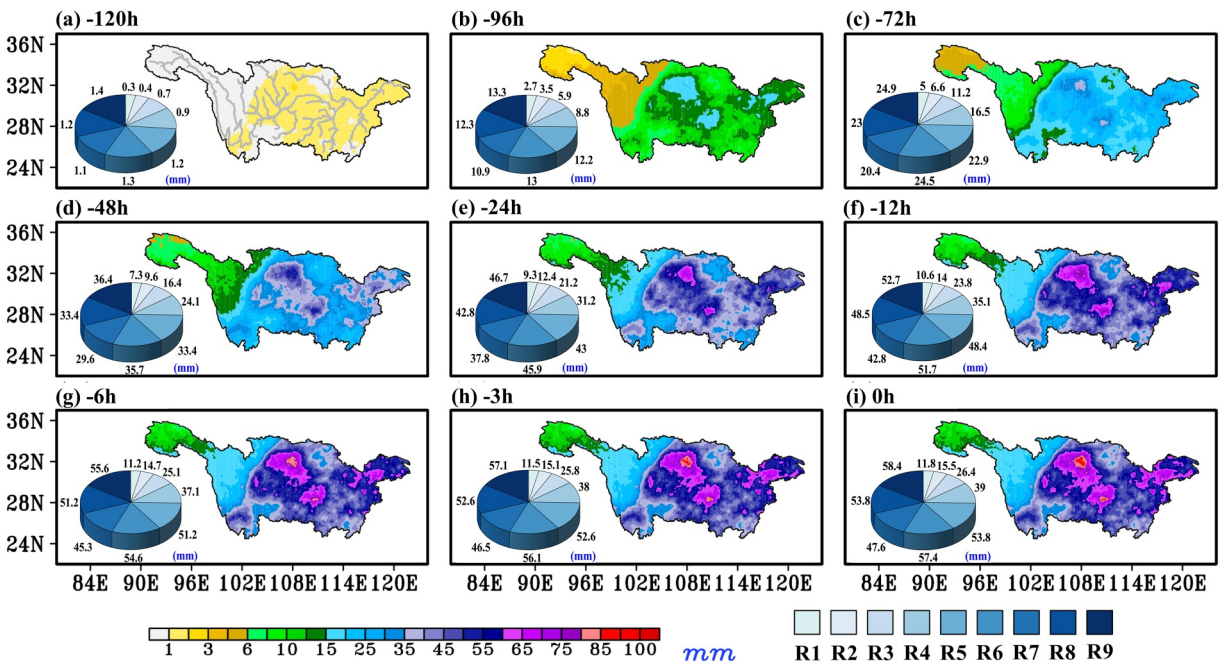

Figure 4. Spatial distribution of cumulative precipitation over the Yangtze River Basin during the 5 days preceding the occurrence of ERDEs for the period 2000–2019. Panel (a) shows precipitation during the initial 3-hr period within the 120 hr preceding ERDEs. The cumulative precipitation in panels (b–i) was calculated starting from 120 hr prior to Extreme River Discharge Event onset up to the specified time.

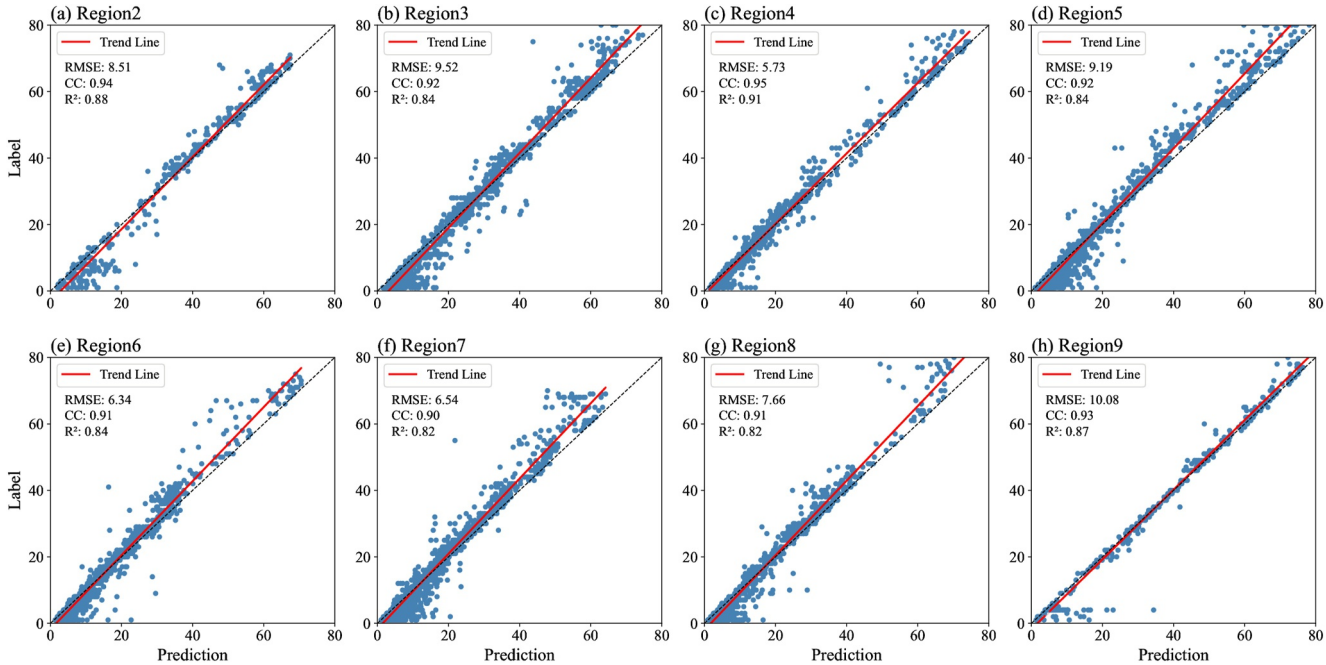

Figure 5. Scatterplots comparing labeled and RF-predicted number of Extreme River Discharge Event occurrences (events) at a 3-hourly resolution for each region of the Yangtze River Basin during 2000–2019. The labeled data are treated as the reference (ground truth) for evaluating prediction performance.

northern Reg5 and southern Reg6 intensified further, forming a core with accumulations >85 mm. Regional mean cumulative precipitation reached 53.8 mm (Reg5), 57.4 mm (Reg6), 53.8 mm (Reg8), and 58.4 mm (Reg9) (Figures 4g and 4h). Notably, a clear spatial correspondence between precipitation maxima and ERDE occurrence was evident only in northern Reg5 and Reg9 (Figures 3b and 4i). This limited spatial coherence suggests that local precipitation alone cannot fully explain the occurrence of ERDEs.

4.3. Assessment of Random Forest Model Performance

Applying the methodology described in Section 3.3, the RF model was trained and validated for Reg2–Reg9, excluding Reg1 due to the absence of an upstream basin. As shown in Figure 5, the model demonstrated strong predictive performance across all regions, with CC > 0.9, R^2 > 0.82, and RMSE <10 events. All regression relationships were statistically significant at the 99% confidence level. These results indicate that the RF model effectively captured the relationship between the regional cumulative number of ERDE occurrences and local/upstream cumulative precipitation during the 5 days preceding ERDEs.

The proposed framework can be extended to other river basins to investigate ERDE-related precipitation patterns and underlying meteorological mechanisms, provided that terrain characteristics, river gradients, and upstream–downstream connectivity are explicitly considered. However, applying this approach elsewhere may be challenged by basin-specific hydrological conditions, reservoir regulation, and coarse-resolution or sparsely sampled precipitation and river discharge data sets. Additionally, the RF input features and the temporal/spatial resolution may require adjustment, and circulation diagnostics should be tailored to dominant regional weather systems.

4.4. Precipitation Patterns Associated With ERDEs Based on the Random Forest Model

The precipitation patterns associated with ERDEs in the YRB can be classified into three types—local, upstream, and overlapped—based on the feature importance ranking from the RF model. Eastern Tibetan Plateau (Reg2) and Dongting Lake Plain (Reg7) exhibited the upstream precipitation pattern. In these regions, cumulative upstream precipitation at the time of ERDE occurrence (PU0h) demonstrated the highest feature importance over the 5 days preceding ERDEs (Figures 6a and 6g), strongly suggesting that ERDEs in these areas were primarily driven by upstream precipitation processes. In Reg2, high-frequency ERDE occurrences were predominantly concentrated in its northwestern part (30°N–34°N, 95°E–98°E). This spatial clustering can be attributed to the

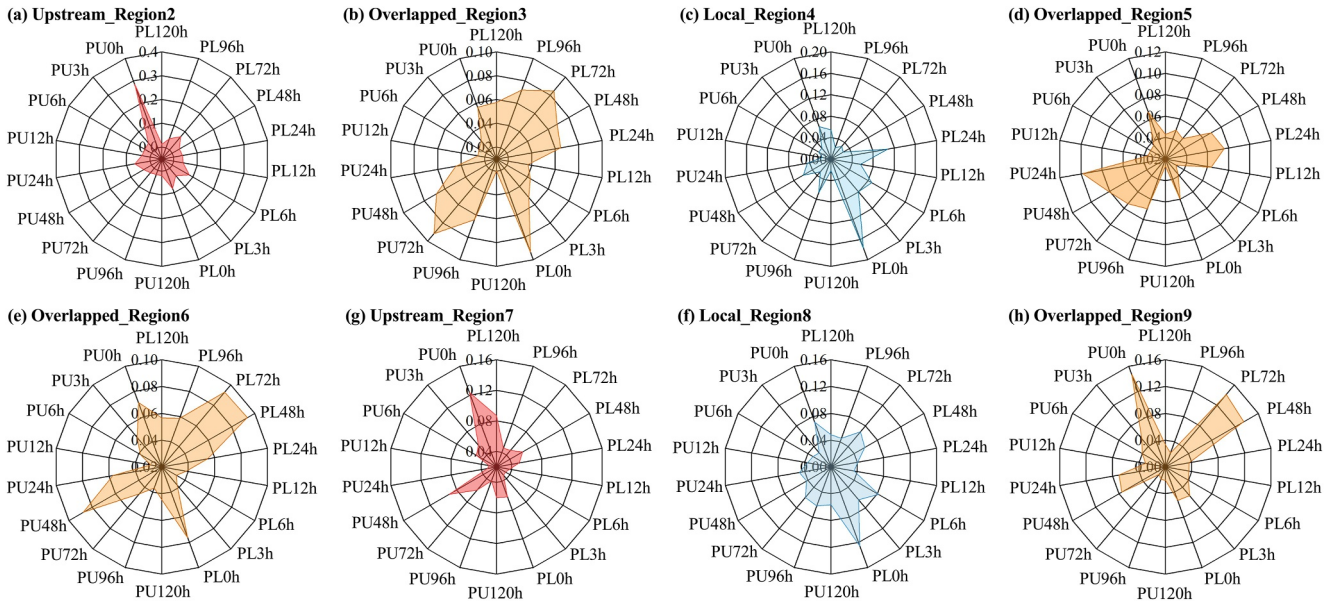

Figure 6. Radar maps of the feature importance of cumulative precipitation at different lead times associated with the cumulative number of Extreme River Discharge Event occurrences, based on the RF model. Red, blue, and yellow represent upstream, local, and overlapped precipitation pattern types, respectively.

steep river gradients and high average discharge observed during ERDEs, which increase the region's sensitivity to upstream precipitation (Figures 1b and 3c). Similarly, in Reg7, the influence of Wushan Mountain and the steep upstream topography create favorable conditions for water accumulation, reinforcing the dominance of the upstream precipitation pattern in this region (Figures 1b and 3c).

The precipitation patterns associated with ERDEs in the Western Sichuan Basin (Reg4) and Poyang Lake Plain (Reg8) were classified as the local type, characterized by the dominant contribution of cumulative local precipitation during the 5 days preceding ERDEs (PL0h) (Figures 6c and 6f). This finding indicates that ERDEs over these regions were primarily driven by local precipitation processes. Reg4 receives an annual mean precipitation exceeding 1,000 mm, making it one of China's major rainfall centers (Fu et al., 2020). This high precipitation is primarily attributed to the orographic blocking effect of the Tibetan Plateau, which enhances local precipitation. In contrast, Reg8 is characterized by flat terrain, gentle river slopes, and a dense tributary network, along with high river discharge during ERDEs (Figures 1 and 3c). These geomorphological and hydrological features promote rapid runoff routing and limit water storage, suggesting that ERDEs in Reg8 are primarily controlled by local precipitation rather than upstream inputs.

The precipitation patterns associated with ERDEs in the Western Sichuan Plateau (Reg3), Central-eastern Sichuan Basin (Reg5), Wushan Mountain Range (Reg6), and Lower Yangtze River Plain (Reg9) were classified as the overlapped type, indicating that ERDEs in these regions were jointly influenced by upstream and local precipitation contributions. These regions were characterized by complex interactions between terrain and atmospheric circulation, creating a dynamic environment in which both upstream and local precipitation played significant roles in triggering ERDEs (Figures 6b, 6d, 6e, and 6h). Overall, the precipitation patterns associated with ERDEs across the YRB exhibit pronounced spatial heterogeneity, primarily driven by variability in regional weather systems. These findings underscore the importance of further investigating the underlying atmospheric mechanisms that govern the relationship between precipitation processes and ERDE occurrence.

4.5. Atmospheric Circulation Associated With ERDE-Related Precipitation Patterns

This section investigates the meteorological mechanisms underlying different precipitation patterns associated with ERDEs. Unstable atmospheric stratification, ascending air motion, abundant water vapor transport, and adequate cloud condensation nuclei are key factors contributing to precipitation formation (Peters & Neelin, 2006). Here, we focus on the first three factors and examine how they shape the precipitation patterns associated with ERDEs.

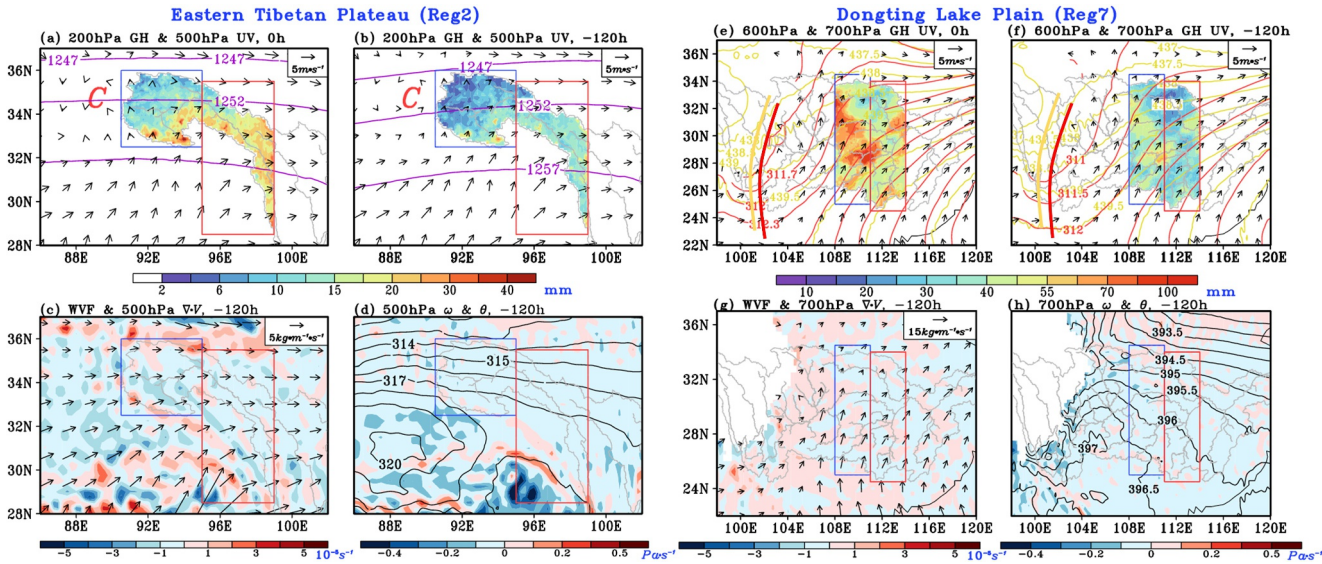

Figure 7. Atmospheric circulation and physical features associated with the upstream-type precipitation pattern. The shading illustrates (a) cumulative precipitation during the 120 hr preceding ERDEs and (b) precipitation during the initial 3-hr period within this 120-hr window in Reg2. Purple contours depict the geopotential height (dagpm) at 200 hPa, vectors represent the wind fields (m s^{-1}) at 500 hPa, and the red "C" symbolizes the Tibetan Plateau Vortex. (c) Vertically integrated (surface–300 hPa) water vapor flux (vectors; kg m^{-1} s^{-1}) and divergence (shading; 10^{-5} s^{-1}), and (d) vertical velocity (shading; Pa s^{-1}) with 500-hPa PEPT (contours; (K), shown initial 3-hr period within the 120 hr preceding an Extreme River Discharge Event in Reg2. Red and blue rectangles denote the local and upstream regions, respectively. (e, f) Same as (a, b), but showing geopotential height at 600 hPa (yellow contours) and 700 hPa (red contours), and 700-hPa wind fields; red (yellow) solid lines indicate backward-tilting troughs over Reg7. (g, h) Same as (c, d), but at 700 hPa over Reg7.

4.5.1. Atmospheric Circulation Associated With the Upstream-Type Precipitation Pattern

ERDEs in Eastern Tibetan Plateau (Reg2) exhibited pronounced spatial clustering in the northwestern sector (30° N–34°N, 95°E–98°E), coinciding with the maximum precipitation center observed during the 5 days preceding the events (Figures 3b and 7a). At 120 hr before ERDE onset in Reg2, an apparent Tibetan Plateau vortex was observed at 500 hPa, centered over 34°N–36°N, 88°E–90°E, west of Reg1, the upstream region of Reg2. This mesoscale system dynamically interacted with the periphery of the South Asian High at 200 hPa, creating strong upper-level divergence that enhanced low-level air uplift (Figure 7b). The Tibetan Plateau vortex induced persistent southwesterly winds at 500 hPa over southeastern Reg1 and much of Reg2, significantly enhancing water vapor transport (Figure 7c). Diagnostic analyses indicated pronounced convergence (divergence $<-3\times10^{-5}$ s^{-1}) and upward motion (vertical velocities <-0.1 Pa s^{-1}) across these regions, providing favorable dynamic conditions for precipitation development (Figures 7c and 7d). Further evidence of atmospheric instability was apparent in the 500 hPa PEPT field, which featured a warm core near 31°N, 89°E with an eastward-protruding ridge (Figure 7d). Thus, the eastward-propagating Tibetan Plateau vortex systematically shifted precipitation from its origin in Reg1 downstream to Reg2, explaining the formation mechanism of the upstream-type precipitation pattern observed in Reg2.

ERDEs in Dongting Lake Plain (Reg7) exhibited distinct spatial clustering along both the northern and southern main river channels (Figure 3b). Notably, the 5-day cumulative precipitation preceding these events was predominantly concentrated over Wushan Mountain Range (Reg6) and along the Reg6–Reg7 boundary (Figure 7e). At 120 hr before the ERDE onset in Reg7, a backward-tilting trough was observed at 700 hPa near 104°E, characterized by a geopotential height trough sloping to the southwest with height. In front of the backward-tilting trough (east of 104°E), prevailing southwesterly winds transported abundant water vapor toward Reg6 and Reg7 at 700 hPa (Figure 7f). Meanwhile, strong lower-tropospheric convergence (horizontal divergence $<-2\times10^{-5}$ s^{-1}) and pronounced upward motion (vertical velocity <-0.2 Pa s^{-1}) established favorable dynamic conditions for precipitation development (Figures 7g and 7h). The 700 hPa PEPT ridge (the ridge line formed by the large value area of PEPT) field showed a northward-extending ridge near 105°E, indicating continued intensification and maintenance of the backward-tilting trough structure (Figure 7h). This synoptic configuration induced prolonged precipitation events over Reg6, explaining that ERDEs in Reg7 were mainly dominated by

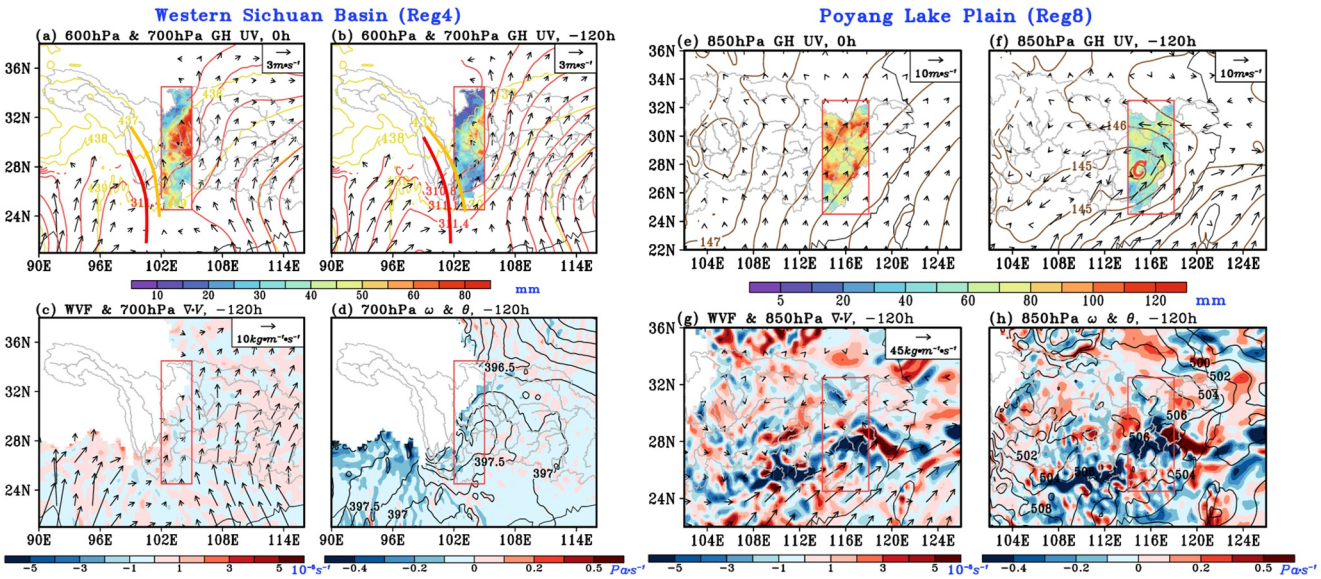

Figure 8. Same as Figure 7, but shown for Reg4 and Reg8. Red and Yellow solid lines in (a, b) symbolize the forward-tilting trough at 700 hPa and 600 hPa, respectively, and brown contours in (e, f) depict the geopotential height (contour; dagpm) at 850 hPa. The red "C" in (f) signifies the Jianghuai cyclone at 850 hPa.

sustained upstream precipitation processes. Overall, ERDEs driven by upstream precipitation primarily occur because the responsible weather systems develop over the upstream region as early as 5 days before the event.

4.5.2. Atmospheric Circulation Associated With the Local-Type Precipitation Pattern

ERDEs in Western Sichuan Basin (Reg4) were primarily concentrated along the southern section of the mainstream, and the 5-day cumulative precipitation ahead of ERDEs concentrated in the central Reg4 (Figures 3b and 8a). At 120 hr prior to ERDE onset, a forward-tilting trough was observed at 700 hPa, centered near 102°E. This system was characterized by a geopotential height trough sloping northeastward with height (Figure 8b). To the east of the trough, prevailing southerly winds transported abundant water vapor to Reg4 (Figures 8b and 8c). Moreover, water vapor enhanced convergence and uplift over the region, with the divergence and vertical velocity at 700 hPa declining to -2×10^{-5} s^{-1} and -0.3 Pa s^{-1}, respectively, over the western Sichuan Basin (Figures 8c and 8d). The 700-hPa PEPT field featured a prominent warm core over this region, further supporting sustained ascending motion and indicating a high probability of persistent heavy precipitation (Figure 8d). These findings demonstrate that ERDEs in Reg4 were predominantly controlled by local precipitation processes.

ERDEs in Poyang Lake Plain (Reg8) were concentrated on the mainstream of the Yangtze River (Figure 3b). This distribution corresponded with two major precipitation centers observed during the 5 days preceding ERDEs, located in northern and central Reg8 near the river's mainstream (Figure 8e). At 120 hr ahead of ERDEs, a Jianghuai cyclone system developed at 850 hPa over central Reg8 (27°N–28°N, 113°E–115°E) (Figure 8f). The Jianghuai cyclone is a mesoscale extratropical cyclone that develops over the Yangtze-Huaihe River Basin (30°N–35°N, 110°E–120°E) during late spring and early summer, playing a key role in triggering heavy rainfall and severe convective weather over eastern China (Zhu & Chen, 2024). This mesoscale system established strong southwesterly winds at 850 hPa across Reg8, transporting abundant water vapor from the South China Sea. The Jianghuai cyclone also generated an intense convergence center with divergence below -5×10^{-5} s^{-1} near 27°N, 115°E (Figure 8g). A high-value center of the PEPT was distributed around the core of the low-level Jianghuai cyclone at 850 hPa, indicating significant atmospheric instability. The cyclone further induced air ascending with a vertical velocity lower than -0.4 Pa s^{-1}, resulting in locally heavy precipitation (Figure 8h). These findings indicate that ERDEs in Reg8 were dominated by local precipitation. Overall, in regions where ERDEs are primarily driven by local precipitation, the responsible weather systems induce rainfall within the local area up to 5 days before the event.

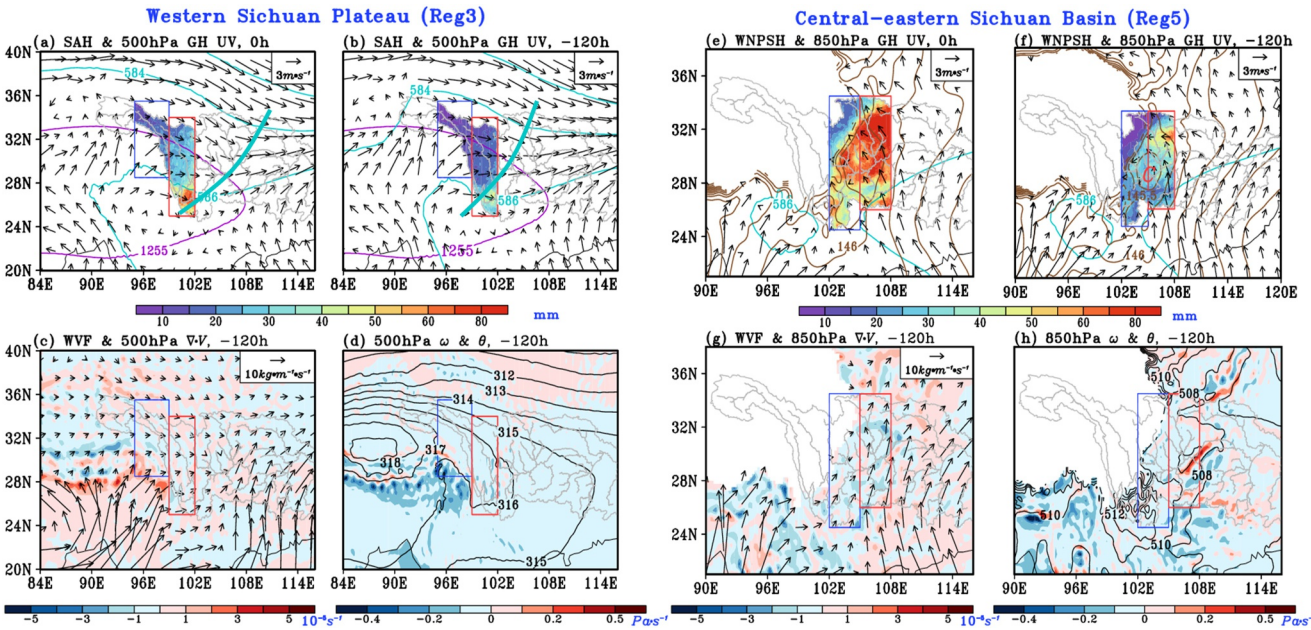

Figure 9. Same as Figure 7, but shown for Reg3 and Reg5. Blue and brown contours in (a, b) and (e, f) denote the geopotential height (contour; dagpm) at 500 hPa and 850 hPa, respectively. The blue solid line in (a, b) signifies the westerly trough, and the red "C" in (f) symbolizes the southwest vortex at 850 hPa.

4.5.3. Atmospheric Circulation Associated With the Overlapped-Type Precipitation Pattern

ERDEs in Western Sichuan Plateau (Reg3) were primarily concentrated along the southern segment of the main river channel, closely aligning with the spatial distribution of cumulative precipitation during the 5 days preceding ERDEs (Figures 3b and 9a). At 120 hr ahead of ERDEs, a westerly trough emerged over the eastern Tibetan Plateau at 500 hPa, while the South Asian High at 200 hPa covered the southern Tibetan Plateau. The upper-tropospheric divergence associated with the South Asian High enhanced air convergence ahead of the westerly trough (east of 98°E) at 500 hPa (Figure 9b). Under the influence of the westerly trough, southwesterly winds dominated much of Reg3 and its boundary with Reg2, facilitating substantial water vapor transport into the region (Figure 9c). The divergence and vertical velocity at 500 hPa dropped below -2×10^{-5} s^{-1} and -0.2 Pa s^{-1}, respectively, indicating strong upward motion and convergence of moist air (Figures 9c and 9d). Moreover, a warm tongue of the PEPT extended from Reg2 to Reg3, reflecting the sustained presence and gradual eastward progression of the westerly trough and the associated shift of precipitation from Reg2 to Reg3 (Figure 9d). These results suggest that ERDEs in Reg3 were influenced by a combination of upstream and local precipitation processes.

ERDEs in Central-eastern Sichuan Basin (Reg5) were distributed across the northern part of the region, closely corresponding with areas of high cumulative precipitation during the 5 days preceding the events (Figures 3b and 9e). The spatial pattern of cumulative precipitation showed a west-to-east increasing gradient across Reg5 and its upstream area (Reg4) (Figure 9e). At 120 hr before the ERDEs, a southwest vortex system at 850 hPa was identified near the junction of Reg5 and Reg4, centered around 28°N, 104°E (Figure 9f). Meanwhile, the Western North Pacific Subtropical High (WNPSH), located south of Reg5 at 500 hPa, facilitated the transport of abundant water vapor from the Bay of Bengal toward both Reg5 and Reg4 (Figures 9f and 9g). The divergence and vertical velocity at 850 hPa reached -3×10^{-5} s^{-1} and -0.2 Pa s^{-1}, respectively, over the junction between the two regions, indicating convergent upward air movement (Figures 9g and 9h). The PEPT field exhibited an eastward-extending ridge across southern Reg4, indicating a sustained and eastward-propagating precipitation system from Reg4 to Reg5 (Figure 9h). Thus, ERDEs in Reg5 were driven by a combination of upstream and local precipitation processes.

ERDEs in Wushan Mountain Range (Reg6) occurred most frequently along its northern tributary, aligning with a southwest-northeast-oriented pattern of precipitation accumulation observed in Reg6 and upstream Reg5 during the 5 days preceding the events (Figures 3b and 10a). At 72 hr before the ERDEs, a double vortex system was

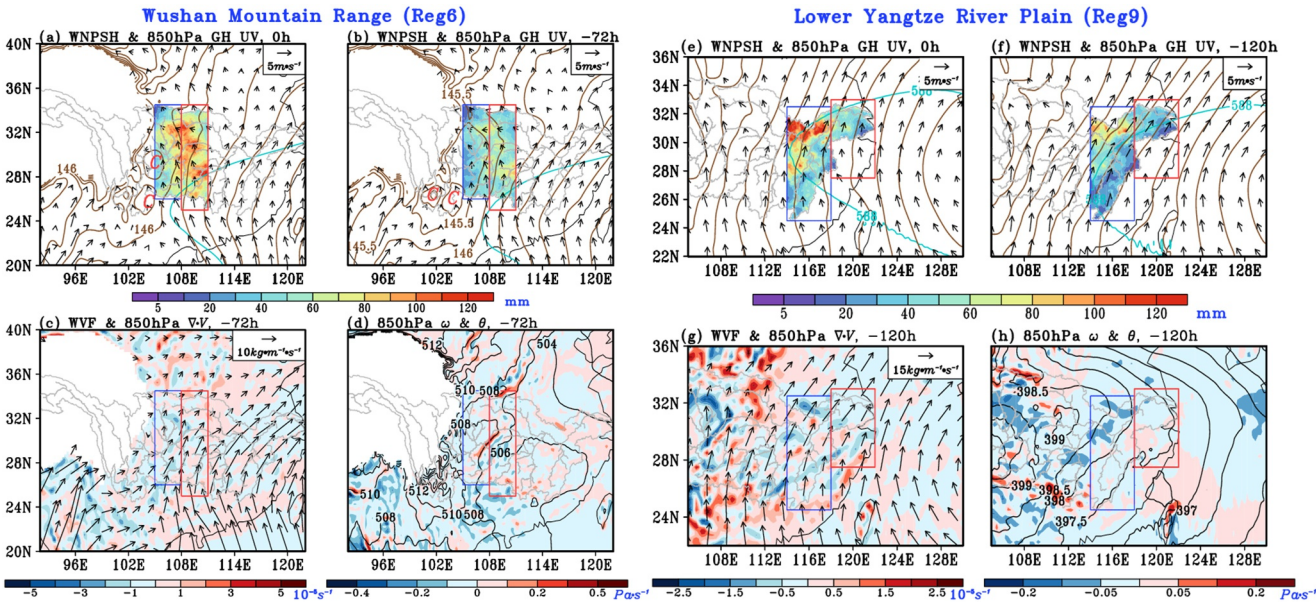

Figure 10. Same as Figure 7, but shown for Reg6 and Reg9. The double red "C" in (a, b) represents the double vortex at 850 hPa. Blue and brown contours in (a, b) and (e, f) denote the geopotential height (contour; dagpm) at 500 hPa and 850 hPa, respectively.

observed west of Reg5 near 25°N–27°N, 101°E–103°E (Figure 10b). With the WNPSH at 500 hPa extending over southern Reg6, abundant water vapor was transported to Reg6 and Reg5, further enhanced by the circulation associated with the double vortex (Figures 10b and 10c). In the middle of Reg5 and Reg6, dynamic conditions were favorable for precipitation development, with divergence and vertical velocity at 850 hPa reaching -2×10^{-5} s^{-1} and -0.2 Pa s^{-1}, respectively, indicating strong convergence and upward motion of water vapor (Figures 10c and 10d). Additionally, a warm tongue in the PEPT field extended from Reg5 into central Reg6, indicating a northeastward shift in precipitation associated with the northwestward movement of the double vortex system (Figure 10d). Therefore, ERDEs in Reg6 were influenced by both upstream and local precipitation processes. Compared with a single vortex, a double vortex requires more abundant water vapor transport and stronger dynamic uplift, and it typically has a relatively short lifespan (Jin et al., 2019; Tang et al., 2023). Accordingly, the double vortex in Reg6 tends to develop during the later stage of events relative to other regions of the YRB.

ERDEs in the Lower Yangtze River Plain (Reg9) were primarily concentrated along the mainstream (Figure 3b). The spatial distribution of cumulative precipitation during the 5 days preceding these events was mainly located in the upstream region, particularly along the mainstream of Reg8 (Figure 10e). At 120 hr before the ERDEs, the WNPSH extended to 32N°. Under the influence of prevailing southwesterly winds at 500 hPa, the northern portion of the upper reached in Reg9 received abundant water vapor (Figures 10f and 10g). Moreover, divergence and vertical velocity in this area dropped below -1.5×10^{-5} s^{-1} and -0.2 Pa s^{-1}, respectively, indicating strong convergence and upward transport of water vapor (Figures 10g and 10h). The ridge line of PEPT also extended from west to east across Reg9 and Reg8, suggesting an eastward movement of the precipitation system (Figure 10h). Consequently, ERDEs in Reg9 were influenced by both upstream and local precipitation processes.

In general, during the 5 days preceding ERDEs over the YRB from 2000 to 2019, atmospheric circulation signals of precipitation systems varied with precipitation-pattern type (Table 1). For the upstream-type precipitation pattern, the responsible system was typically located to the west of the upstream region. For the local-type pattern, the weather system was situated within the local region and occasionally extended into the upstream area. For the overlapped pattern, the precipitation system was generally located near the junction of the local and upstream regions and propagated eastward.

Table 1
Precipitation Patterns and Corresponding Atmospheric Circulation Signals Associated With ERDEs Across Regions of the YRB

Regions	Precipitation patterns	Atmospheric circulation signals
Reg2	Upstream type	South Asia High and Tibetan Plateau Vortex
Reg3	Overlapped type	South Asia High and Westerly Trough
Reg4	Local type	Forward-tilting Trough
Reg5	Overlapped type	Southwest Vortex
Reg6	Overlapped type	Double Vortex
Reg7	Upstream type	Backward-tilting Trough
Reg8	Local type	Jianghuai Cyclone
Reg9	Overlapped type	Convective Precipitation at the Edge of the WNPSH

5. Conclusions

Understanding the spatiotemporal distribution, precipitation patterns, and associated meteorological mechanisms of ERDEs is essential for identifying early warning signals of potential flooding. In this study, we investigated the characteristics of ERDEs over the YRB from 2000 to 2019. Based on an RF model, we quantified the relationship between the cumulative number of ERDE occurrences and cumulative precipitation. Furthermore, we identified three dominant precipitation patterns and analyzed the relative atmospheric processes. The main conclusions are summarized as follows:

1. ERDEs occurred frequently in the eastern Tibetan Plateau and the middle to lower reaches of the YRB, with a regional mean cumulative number of ERDE occurrences exceeding 80 events. Temporally, ERDEs occurred from March to November, peaking in summer, particularly in July, with an annual average of 129.3 events across the YRB during 2000–2019. Notably, the occurrence of ERDEs exhibited a significant upward trend, increasing by an average of 17.5 events per year from 2000 to 2019.
2. Precipitation patterns associated with ERDEs during 2000–2019 were categorized into three types: upstream, local, and overlapped. Upstream-dominated ERDEs were found in the eastern Tibetan Plateau (Reg2) and Dongting Lake Plain (Reg7). Local precipitation dominated ERDEs in the western Sichuan Basin (Reg4) and Poyang Lake Plain (Reg8). Overlapped influences (both upstream and local) affected ERDEs in the western Sichuan Plateau (Reg3), central-eastern Sichuan Basin (Reg5), Wushan Mountain Range (Reg6), and the lower Yangtze River Plain (Reg9).
3. The atmospheric systems affecting the precipitation patterns of ERDEs were typically observed 72–120 hr before event onset. Progressing from west to east along the YRB, these systems include: a plateau vortex at 500 hPa (Reg2), a westerly trough at 500 hPa (Reg3), a forward-tilting trough (Reg4), a southwest vortex at 700 hPa (Reg5), a double vortex at 850 hPa (Reg6), a backward-tilting trough (Reg7), a Jianghuai cyclone at 850 hPa (Reg8), and a convective system on the western edge of the WNPSH at 500 hPa (Reg9).
4. The roles of soil moisture, reservoir distribution, and land-surface properties in modulating ERDEs warrant further investigation. Future research should therefore focus on representative regions and longer-term data sets to clarify the physical linkages among atmospheric circulation, surface hydrological responses, and ERDE occurrence. Building on the quantified relationships between precipitation patterns and ERDEs, more robust and reliable predictive models can be developed.

Conflict of Interest

The authors declare no conflicts of interest relevant to this study.

Availability Statement

The data sets used in this study are described as follows: the river order and slope information (https://hydro.iis.u-tokyo.ac.jp/~yamadai/MERIT_Hydro/) were derived from the MERIT_Hydro_v07_Basins_v01 data set (Yamazaki et al., 2019). River discharge data (https://www.reachhydro.org/home/records/grfr) were obtained

from the Global Reach-Level 3-Hourly River Flood Reanalysis (Yang, Pan, et al., 2021). Precipitation data (https://gpm.nasa.gov/data/imerg) were sourced from the final run of the GPM-IMERG V06 data set (Hou et al., 2014). Historical flood event records for comparison data were obtained from the Global Natural Disaster Information Database (http://disaster.ncdc.ac.cn/#/root/view), maintained by the National Cryosphere Desert Data Center of China. Atmospheric variables were from the fifth-generation ECWMF reanalysis data set (https://cds.climate.copernicus.eu/datasets/reanalysis-era5-pressure-levels?tab=overview), which was accessed through the Copernicus Climate Change Service (C3S) Climate Data Store (CDS) (Hersbach et al., 2023). Topography information (https://developers.google.com/earth-engine/datasets/catalog/CGIAR_SRTM90_V4) was derived from the Shuttle Radar Topography Mission Digital Elevation Database v4.1 (Jarvis et al., 2008).

Acknowledgments
We thank Dr. Yang Yuan from Princeton University for kindly addressing questions regarding the GRFR data set. This work was supported by the National Natural Science Foundation of China (42505025, 42201349, 42571446, and 42501416), the National Open Fund for Rainstorm Research (BYKJ2024Q02), and the Chongqing Municipal Science and Technology Bureau (CSTB2024YCJH-KYXM0054 and cstc2024ycjh-bgzxm0043), the Postdoctoral Innovation Talents Support Program of Chongqing (CQBX202322), and the Postdoctoral Fellowship Program of CPSF (GZC20232172).

References

Adikari, K. E., Shrestha, S., Ratnayake, D. T., Budhathoki, A., Mohanasundaram, S., & Dailey, M. N. (2021). Evaluation of artificial intelligence models for flood and drought forecasting in arid and tropical regions. *Environmental Modelling & Software*, *144*, 105136. https://doi.org/10.1016/j.envsoft.2021.105136

Bai, L., Chen, G., Huang, Y., & Meng, Z. (2021). Convection initiation at a coastal rainfall hotspot in South China: Synoptic patterns and orographic effects. *Journal of Geophysical Research: Atmospheres*, *126*(24), e2021JD034642. https://doi.org/10.1029/2021JD034642

Belgiu, M., & Drăguţ, L. (2016). Random forest in remote sensing: A review of applications and future directions. *ISPRS Journal of Photogrammetry and Remote Sensing*, *114*, 24–31. https://doi.org/10.1016/j.isprsjprs.2016.01.011

Bolton, D. (1980). The computation of equivalent potential temperature. *Monthly Weather Review*, *108*(7), 1046–1053. https://doi.org/10.1175/1520-0493(1980)108<1046:TCOEPT>2.0.CO;2

Breiman, L. (2001). Random forests. *Machine Learning*, *45*(1), 5–32. https://doi.org/10.1023/A:1010933404324

Breinl, K., Lun, D., Müller-Thomy, H., & Blöschl, G. (2021). Understanding the relationship between rainfall and flood probabilities through combined intensity-duration-frequency analysis. *Journal of Hydrology*, *602*, 126759. https://doi.org/10.1016/j.jhydrol.2021.126759

Breugem, A. J., Wesseling, J. G., Oostindie, K., & Ritsema, C. J. (2020). Meteorological aspects of heavy precipitation in relation to floods–an overview. *Earth-Science Reviews*, *204*, 103171. https://doi.org/10.1016/j.earscirev.2020.103171

Camilloni, I. A., & Barros, V. R. (2003). Extreme discharge events in the Paraná River and their climate forcing. *Journal of Hydrology*, *278*(1–4), 94–106. https://doi.org/10.1016/S0022-1694(03)00133-1

Chen, J., Wu, X., Finlayson, B. L., Webber, M., Wei, T., Li, M., & Chen, Z. (2014). Variability and trend in the hydrology of the Yangtze River, China: Annual precipitation and runoff. *Journal of Hydrology*, *513*, 403–412. https://doi.org/10.1016/j.jhydrol.2014.03.044

Deng, P., Zhang, M., Hu, Q., Wang, L., & Bing, J. (2022). Pattern of spatio-temporal variability of extreme precipitation and flood-waterlogging process in Hanjiang River basin. *Atmospheric Research*, *276*, 106258. https://doi.org/10.1016/j.atmosres.2022.106258

Ding, Y., Zhu, Y., Feng, J., Zhang, P., & Cheng, Z. (2020). Interpretable spatio-temporal attention LSTM model for flood forecasting. *Neurocomputing*, *403*, 348–359. https://doi.org/10.1016/j.neucom.2020.04.110

Do, H. X., Mei, Y., & Gronewold, A. D. (2020). To what extent are changes in flood magnitude related to changes in precipitation extremes? *Geophysical Research Letters*, *47*(18), e2020GL088684. https://doi.org/10.1029/2020GL088684

Durowoju, O. S., Olusola, A. O., & Anibaba, B. W. (2017). Relationship between extreme daily rainfall and maximum daily river discharge within Lagos metropolis. *Ethiopian Journal of Environmental Studies & Management*, *10*(4), 492–504. https://doi.org/10.4314/ejesm.v10i4.7

Fang, J., Kong, F., Fang, J., & Zhao, L. (2018). Observed changes in hydrological extremes and flood disaster in Yangtze River Basin: Spatial–temporal variability and climate change impacts. *Natural Hazards*, *93*(1), 89–107. https://doi.org/10.1007/s11069-018-3290-3

Fu, S., Li, W., Sun, J., Zhang, J., & Zhang, Y. (2015). Universal evolution mechanisms and energy conversion characteristics of long-lived mesoscale vortices over the Sichuan Basin. *Atmospheric Science Letters*, *16*(2), 127–134. https://doi.org/10.1002/asl2.533

Fu, S., Sun, J., Zhao, S., & Li, W. (2011). The energy budget of a southwest vortex with heavy rainfall over South China. *Advances in Atmospheric Sciences*, *28*(3), 709–724. https://doi.org/10.1007/s00376-010-0026-z

Fu, Y., Ma, Y., Zhong, L., Yang, Y., Guo, X., Wang, C., et al. (2020). Land-surface processes and summer-cloud-precipitation characteristics in the Tibetan Plateau and their effects on downstream weather: A review and perspective. *National Science Review*, *7*(3), 500–515. https://doi.org/10.1093/nsr/nwz226

Gao, S., Ti, C. P., Tang, S. R., Wang, X. L., Wang, H. Y., Meng, L., & Yan, X. Y. (2023). Runoff simulation and its response to extreme precipitation in the Yangtze River Basin. *Huan Jing ke Xue Huanjing Kexue (Chinese)*, *44*(9), 4853–4862. https://doi.org/10.13227/j.hjkx.202210150

Heinrich, P., Hagemann, S., Weisse, R., Schrum, C., Daewel, U., & Gaslikova, L. (2023). Compound flood events: Analysing the joint occurrence of extreme river discharge events and storm surges in northern and central Europe. *Natural Hazards and Earth System Sciences*, *23*(5), 1967–1985. https://doi.org/10.5194/nhess-23-1967-2023

Hersbach, H., Bell, B., Berrisford, P., Biavati, G., Horányi, A., et al. (2023). ERA5 monthly averaged data on single levels from 1940 to present [Dataset]. *Copernicus Climate Change Service (C3S) Climate Data Store (CDS)*. https://cds.climate.copernicus.eu/datasets/reanalysis-era5-pressure-levels?tab=overview

Hou, A. Y., Kakar, R. K., Neeck, S., Azarbarzin, A. A., Kummerow, C. D., Kojima, M., et al. (2014). The global precipitation measurement mission. *Bulletin of the American Meteorological Society*, *95*(5), 701–722. https://doi.org/10.1175/BAMS-D-13-00164.1

Hua, S., Xu, X., & Chen, B. (2020). Influence of multiscale orography on the initiation and maintenance of a precipitating convective system in North China: A case study. *Journal of Geophysical Research: Atmospheres*, *125*(13), e2019JD031731. https://doi.org/10.1029/2019JD031731

Jarvis, A., Reuter, H. I., Nelson, A., & Guevara, E. (2008). The Shuttle radar topography mission (SRTM) 90m digital elevation database v4.1 [Dataset]. *CGIAR Consortium for Spatial Information*. https://developers.google.com/earth-engine/datasets/catalog/CGIAR_SRTM90_V4

Jia, H., Chen, F., Pan, D., Du, E., Wang, L., Wang, N., & Yang, A. (2022). Flood risk management in the Yangtze River basin—Comparison of 1998 and 2020 events. *International Journal of Disaster Risk Reduction*, *68*, 102724. https://doi.org/10.1016/j.ijdrr.2021.102724

Jin, X., Lv, W., Lv, X., Tang, Z., & Chen, Q. (2019). Cause analysis of a double-cyclone type of rainstorm process with easterly wave. *Meteorological and Environmental Research*, *10*(2), 15–26. https://doi.org/10.19547/j.issn2152-3940.2019.02.003

Kang, Y., Peng, X., Wang, S., Hu, Y., Shang, K., & Lu, S. (2019). Observational analyses of topographic effects on convective systems in an extreme rainfall event in Northern China. *Atmospheric Research*, *229*, 127–144. https://doi.org/10.1016/j.atmosres.2019.05.024

Kundzewicz, Z. W., Huang, J., Pinskwar, I., Su, B., Szwed, M., & Jiang, T. (2020). Climate variability and floods in China-A review. *Earth-Science Reviews*, *211*, 103434. https://doi.org/10.1016/j.earscirev.2020.103434

Kundzewicz, Z. W., Su, B., Wang, Y., Xia, J., Huang, J., & Jiang, T. (2019). Flood risk and its reduction in China. *Advances in Water Resources*, *130*, 37–45. https://doi.org/10.1016/j.advwatres.2019.05.020

Li, C., Sun, N., Lu, Y., Guo, B., Wang, Y., Sun, X., & Yao, Y. (2022). Review on urban flood risk assessment. *Sustainability*, *15*(1), 765. https://doi.org/10.3390/su15010765

Li, M., Ma, Z., & Lv, M. (2017). Variability of modeled runoff over China and its links to climate change. *Climatic Change*, *144*(3), 433–445. https://doi.org/10.1007/s10584-015-1593-x

Li, W., Kang, Y., Li, L., Gao, R., Shu, Z., & Song, S. (2024). Comprehensive assessment of five near-real-time satellite precipitation products in the Lower Yangtze River Basin and the Lixiahe region, China: Dual perspectives from time series and extreme events. *Atmospheric Research*, *308*, 107520. https://doi.org/10.1016/j.atmosres.2024.107520

Li, Y., & Zhao, S. (2022). Floods losses and hazards in China from 2001 to 2020. *Advances in Climate Change Research*, *18*(2), 154. https://doi.org/10.12006/j.issn.1673-1719.2021.196

Liu, Y., You, M., Zhu, J., Wang, F., & Ran, R. (2019). Integrated risk assessment for agricultural drought and flood disasters based on entropy information diffusion theory in the middle and lower reaches of the Yangtze River, China. *International Journal of Disaster Risk Reduction*, *38*, 101194. https://doi.org/10.1016/j.ijdrr.2019.101194

Luu, C., von Meding, J., & Mojtahedi, M. (2019). Analyzing Vietnam's national disaster loss database for flood risk assessment using multiple linear regression-TOPSIS. *International Journal of Disaster Risk Reduction*, *40*, 101153. https://doi.org/10.1016/j.ijdrr.2019.101153

Min, M., Bai, C., Guo, J., Sun, F., Liu, C., Wang, F., et al. (2018). Estimating summertime precipitation from Himawari-8 and global forecast system based on machine learning. *IEEE Transactions on Geoscience and Remote Sensing*, *57*(5), 2557–2570. https://doi.org/10.1109/tgrs.2018.2874950

Nie, Y., & Sun, J. (2021). Synoptic-Scale circulation precursors of extreme precipitation events over Southwest China during the rainy season. *Journal of Geophysical Research: Atmospheres*, *126*(13), e2021JD035134. https://doi.org/10.1029/2021JD035134

Peters, O., & Neelin, J. D. (2006). Critical phenomena in atmospheric precipitation. *Nature Physics*, *2*(6), 393–396. https://doi.org/10.1038/nphys314

Prodhan, F. A., Zhang, J., Hasan, S. S., Sharma, T. P. P., & Mohana, H. P. (2022). A review of machine learning methods for drought hazard monitoring and forecasting: Current research trends, challenges, and future research directions. *Environmental Modelling & Software*, *149*, 105327. https://doi.org/10.1016/j.envsoft.2022.105327

Simmonds, I., Bi, D., & Hope, P. (1999). Atmospheric water vapor flux and its association with rainfall over China in summer. *Journal of Climate*, *12*(5), 1353–1367. https://doi.org/10.1175/1520-0442(1999)012<1353:AWVFAI>2.0.CO;2

Tang, X. D., Xu, W., Cai, W., & Wang, C. (2023). Water vapour multi-vortex structure under the interactions of typhoons and mid-low latitude systems during extreme precipitation in North China. *Advances in Climate Change Research*, *14*(1), 116–125. https://doi.org/10.1016/j.accre.2023.01.006

Tavus, B., Can, R., & Kocaman, S. (2022). A CNN-based flood mapping approach using Sentinel-1 data. *ISPRS Annals of the Photogrammetry, Remote Sensing and Spatial Information Sciences*, *3*, 549–556. https://doi.org/10.5194/isprs-annals-V-3-2022-549-2022

Tuel, A., Schaefli, B., Zscheischler, J., & Martius, O. (2021). On the links between sub-seasonal clustering of extreme precipitation and high discharge in Switzerland and Europe. *Hydrology and Earth System Sciences Discussions*, *26*(10), 2649–2669. https://doi.org/10.5194/hess-26-2649-2022

Wang, Q., Xu, Y., Cai, X., Tang, J., & Yang, L. (2021). Role of underlying surface, rainstorm and antecedent wetness condition on flood responses in small and medium sized watersheds in the Yangtze River Delta region, China. *Catena*, *206*, 105489. https://doi.org/10.1016/j.catena.2021.105489

Wang, X., Xia, J., Zhou, M., Deng, S., & Li, Q. (2022). Assessment of the joint impact of rainfall and river water level on urban flooding in Wuhan City, China. *Journal of Hydrology*, *613*, 128419. https://doi.org/10.1016/j.jhydrol.2022.128419

Wang, Y., Ding, Y., Ye, B., Liu, F., Wang, J., et al. (2013). Contributions of climate and human activities to changes in runoff of the Yellow and Yangtze rivers from 1950 to 2008. *Science China Earth Sciences*, *56*(8), 1398–1412. https://doi.org/10.1007/s11430-012-4505-1

Wei, K., Ouyang, C., Duan, H., Li, Y., Chen, M., Ma, J., et al. (2020). Reflections on the catastrophic 2020 Yangtze River Basin flooding in southern China. *The Innovation*, *1*(2), 100038. https://doi.org/10.1016/j.xinn.2020.100038

Wei, W., Yan, Z., Tong, X., Han, Z., Ma, M., Yu, S., & Xia, J. (2022). Seasonal prediction of summer extreme precipitation over the Yangtze River based on random forest. *Weather and Climate Extremes*, *37*, 100477. https://doi.org/10.1016/j.wace.2022.100477

Wright, D. B., Yu, G., & England, J. F. (2020). Six decades of rainfall and flood frequency analysis using stochastic storm transposition: Review, progress, and prospects. *Journal of Hydrology*, *585*, 124816. https://doi.org/10.1016/j.jhydrol.2020.124816

Xu, H., Taylor, R. G., & Xu, Y. (2011). Quantifying uncertainty in the impacts of climate change on river discharge in sub-catchments of the Yangtze and Yellow River Basins, China. *Hydrology and Earth System Sciences*, *15*(1), 333–344. https://doi.org/10.5194/hess-15-333-2011

Xu, Q., Chen, J., Peart, M. R., Ng, C. N., Hau, B. C., & Law, W. W. (2018). Exploration of severities of rainfall and runoff extremes in ungauged catchments: A case study of Lai Chi Wo in Hong Kong, China. *Science of the Total Environment*, *634*, 640–649. https://doi.org/10.1016/j.scitotenv.2018.04.024

Xu, X., Huang, A., Huang, D., Zhang, Y., Gu, C., Cai, S., et al. (2023). What are the dominant synoptic patterns leading to the summer regional hourly extreme precipitation events over central-eastern Tibetan Plateau and Sichuan Basin? *Geophysical Research Letters*, *50*(5), e2022GL102342. https://doi.org/10.1029/2022GL102342

Xu, X., Huang, A., Zhao, W., Yang, B., Xue, D., & Zhang, Y. (2024). Roles of the Tibetan Plateau and Yunna-Guizhou Plateau in the regional extreme precipitation over Sichuan Basin in summer: A case Study. *Journal of Geophysical Research: Atmospheres*, *129*(3), e2023JD039776. https://doi.org/10.1029/2023JD039776

Yamazaki, D., Ikeshima, D., Sosa, J., Bates, P. D., Allen, G. H., & Pavelsky, T. M. (2019). MERIT Hydro: A high-resolution global hydrography map based on latest topography dataset. *Water Resources Research*, *55*(6), 5053–5073. https://doi.org/10.1029/2019WR024873

Yang, L., Yang, Y., Villarini, G., Li, X., Hu, H., Wang, L., et al. (2021). Climate more important for Chinese flood changes than reservoirs and land use. *Geophysical Research Letters*, *48*(11), e2021GL093061. https://doi.org/10.1029/2021GL093061

Yang, M., Liu, G., Chen, T., Chen, Y., & Xia, C. (2020). Evaluation of GPM IMERG precipitation products with the point rain gauge records over Sichuan, China. *Atmospheric Research*, *246*, 105101. https://doi.org/10.1016/j.atmosres.2020.105101

Yang, P., Xia, J., Luo, X., Meng, L., Zhang, S., Cai, W., & Wang, W. (2021). Impacts of climate change-related flood events in the Yangtze River Basin based on multi-source data. *Atmospheric Research*, *263*, 105819. https://doi.org/10.1016/j.atmosres.2021.105819

Yang, Y., Pan, M., Lin, P., Beck, H. E., Zeng, Z., Yamazaki, D., et al. (2021). Global reach-level 3-hourly river flood reanalysis (1980–2019). *Bulletin of the American Meteorological Society*, *102*(11), E2086–E2105. https://doi.org/10.1175/BAMS-D-20-0057.1

Ye, X., Xu, C. Y., Li, Y., Li, X., & Zhang, Q. (2017). Change of annual extreme water levels and correlation with river discharges in the middle-lower Yangtze River: Characteristics and possible affecting factors. *Chinese Geographical Science*, *27*(2), 325–336. https://doi.org/10.1007/s11769-017-0866-x

Yin, J., Gentine, P., Zhou, S., Sullivan, S. C., Wang, R., Zhang, Y., & Guo, S. (2018). Large increase in global storm runoff extremes driven by climate and anthropogenic changes. *Nature Communications*, *9*(1), 4389. https://doi.org/10.1038/s41467-018-06765-2

Yu, J., Zou, L., Xia, J., Zhang, Y., Zuo, L., & Li, X. (2023). Investigating the spatial–temporal changes of flood events across the Yangtze River Basin, China: Identification, spatial heterogeneity, and dominant impact factors. *Journal of Hydrology*, *621*, 129503. https://doi.org/10.1016/j.jhydrol.2023.129503

Zhang, F., Zhang, Q., & Sun, J. (2021). Initiation of an elevated mesoscale convective system with the influence of complex terrain during Meiyu season. *Journal of Geophysical Research: Atmospheres*, *126*(1), e2020JD033416. https://doi.org/10.1029/2020JD033416

Zhang, L., Liu, Y., Ren, L., Teuling, A. J., Zhu, Y., Wei, L., et al. (2022). Analysis of flash droughts in China using machine learning. *Hydrology and Earth System Sciences*, *26*(12), 3241–3261. https://doi.org/10.5194/hess-26-3241-2022

Zhang, Y., Xue, M., Zhu, K., & Zhou, B. (2019). What is the main cause of diurnal variation and nocturnal peak of summer precipitation in Sichuan Basin, China? The key role of boundary layer low-level jet inertial oscillations. *Journal of Geophysical Research: Atmospheres*, *124*(5), 2643–2664. https://doi.org/10.1029/2018JD029834

Zhao, G., Liu, R., Yang, M., Tu, T., Ma, M., Hong, Y., & Wang, X. (2022). Large-scale flash flood warning in China using deep learning. *Journal of Hydrology*, *604*, 127222. https://doi.org/10.1016/j.jhydrol.2021.127222

Zhu, R., & Chen, L. (2024). Climatic characteristics of the Jianghuai cyclone and its linkage with precipitation during the Meiyu period from 1961 to 2020. *Natural Hazards and Earth System Sciences*, *24*(6), 1937–1950. https://doi.org/10.5194/egusphere-2023-2008-2023